

To Dr. Roussos, Topical Editor

As I noted under Acknowledgements, I am sincerely grateful to the anonymous referees for their careful reading and stimulating remarks. Although I respect the identify of referee #3 as anonymous, I would appreciate knowing his or her contact address to communicate more directly.

Each issue has been addressed in the prescribed Comment/Response format. These responses were highlighted in bold typeface.

Point-by-point replies to the comments raised by Referee #3 is given below.

Comment 1.

>Kadomtsev [1976] was published only in Russian and Japanese.

The Pergamon Press published the English translation of the Kadomtsev's book in 1982 (ISBN-10: 0080250181, ISBN-13: 978-0080250182)

Response

The following sentence was added in Line 497 regarding reference to Kadomtzev (1979), "English edition published in 1982 is available from Pergamon Press".

Comment 2.

>An arrival of low entropy plasma bubbles into the inner magnetosphere [e.g., Dubyagin et al., >2011] may breakdown the last open trajectories of plasma sheet electrons. This may cause N-S >auroras from poleward aurora boundary [Saka et al., JASTP, 145, 114-124, 2016], However, if >enough field line stretching was developed in the midnight magnetosphere prior to the arrival of >the bubble, the plasma bubble may trigger auroras arising out of arc (substorm onset). The latter >case may not be inconsistent with the global dipolarization model of inner magnetosphere >[Merkin et al., 2019] where intensity and occurrence of dipolarization front (DF) may increase >abruptly at substorm onset. These topics will be the subject of future study.

I don't think the author can ignore the work of Dubyagin et al., 2011

(<https://doi.org/10.1029/2011GL047016>) in this paper, because the author directly touches the question of the penetration depth of BBFs, e.g., Lines 234-235: "Consequently, this scenario requires that the BBFs are not necessary to reach inner magnetosphere to trigger the substorm onset at lower latitudes. ". I also strongly suggest to add here another a reference to Shiokawa et al., 1997 (<https://doi.org/10.1029/97GL01062>).

In turn, the work of Merkin et al., 2019 (<https://doi.org/10.1029/2019JA026872>) is completely in accord with the discussed in the paper in Line 400 seminal work by Baumjohann et al., 1999 on the tailward expansion of the global dipolarization. Taking into account that Merkin's work is a significant contribution to the question the author is addressing in the paper, I believe that the author cannot ignore such results in the present paper.

Response

In section 8 "Discussion and summary", new sentences were added in Lines 378-386 to show how the present results are in accord with bubble observations in [Dubyagin et al., 2011] and simulation results in [Merkin et al., 2019] and in [Yang et al., 2012].

Flow braking [Shiokawa et al., 1997] was added to the tailward expansion process of dipolarization region [Baumjohann et al., 1999], Lines 409-411.

Comment 3.

The paper also lacks discussion of current system that couples deeply injected plasma sheet bubbles with the ionosphere. A great contribution on this topic was made by Yang et al., 2012 <https://doi.org/10.1029/2011JA017415> and is ought to be mentioned and discussed in the paper (as least in the discussion section around Line 415).

Response

Please see response to Comment 2.

Line 152: Should tapped be trapped?

tapped -> trapped

Line 423: The statement „No data sets were used in this article.“ is not consistent with the contents of Figures 1, 4 and 7.

Statement was changed. Please refer to Lines 423-424.

1 The increase of curvature radius of geomagnetic field lines preceding a classical
2 dipolarization

3
4
5 Osuke Saka

6 Office Geophysik, Ogoori, 838-0141, Japan
7
8

9 **Abstract**

10 Based on assumptions that substorm field line dipolarization at geosynchronous altitudes is
11 associated with the arrival of high velocity magnetotail flow bursts referred to as Bursty Bulk
12 Flows, we propose following sequence of field line dipolarization: (1) Slow magnetoacoustic
13 wave excited through Ballooning instability by enhanced inflows in pre-onset intervals
14 towards the equatorial plane; (2) In the equatorial plane, slow magnetoacoustic wave
15 stretching of the flux tube in dawn-dusk directions resulting in spreading plasmas in dawn-
16 dusk directions and reduction in the radial pressure gradient in the flux tube. As a
17 consequence of the foregoing processes, the flux tube assumes a new equilibrium geometry
18 in which curvature radius of new field lines increased in the meridian plane suggesting an
19 onset of field line dipolarization. The dipolarization processes associated with changing the
20 curvature radius preceded classical dipolarization caused by reduction of cross-tail currents
21 and pileup of the magnetic fields.

22 Increasing curvature radius induced convection surge in the equatorial plane as well as
23 inductive westward electric fields of the order of mV/m. Electric fields transmitted to the
24 ionosphere produce electromotive force in the E layer for generating field-aligned current
25 system of Bostrom type. This is also equivalent to the creation of an incomplete Cowling
26 channel in the ionospheric E layer by the convection surge.
27
28

29 **1. Introduction**

30 Substorms are spatially localized and temporarily variable processes in the nighttime
31 magnetosphere. It is often difficult to determine onset timing of substorm processes such as
32 magnetotail flow burst, field line dipolarization, and particle injections. To resolve the timing
33 uncertainties, auroras in global satellite images [Nakamura et al., 2001; Miyashita et al.,
34 2009], intensifications of auroral kilometric radiation [Fairfield et al., 1999; Morioka et al.,
35 2010], and dispersionless particle injection in geosynchronous orbit [Birn et al., 1997] were
36 used. Ground Pi2 pulsations are another useful tool for determination of the substorm timing

37 [Sakurai and Saito, 1976; Nagai et al., 1998; Baumjohann et al., 1999]. Particularly, Pi2s in
38 equatorial region exhibited small phase difference ($m < 1$, m denotes azimuthal wave number)
39 across widely separated stations in the equatorial countries [Kitamura et al., 1988],
40 minimizing the timing uncertainties arising from delays in longitudinal propagations. This
41 enabled us accurate onset timing study of substorms using magnetometer data from two
42 remote locations, geosynchronous altitudes and ground stations of the equatorial countries
43 [Saka et al., 2010].

44 In this study, we focus on the dipolarization events at geosynchronous orbit from growth to
45 expansion phase. Triggering mechanisms of the field line dipolarization in the vicinity of
46 geosynchronous orbit are our major concern. In this paper, onset timing study of substorms
47 using magnetometer data from equatorial countries are summarized in Sect. 2. In Sect. 3,
48 we present a pre-onset scenario leading to the dipolarization onset. In Sect. 4, excitation of
49 slow magnetoacoustic wave is discussed for triggering field line depolarization. We will focus
50 on the field line dipolarization in the vicinity of geosynchronous orbit in Sect. 5. A coupling of
51 magnetosphere and ionosphere associated with this dipolarization scenario will be presented
52 in Sect. 6. In Sect. 7, we present a triggering mechanism of low latitude Pi2s that enabled
53 the Pi2-based epoch analyses. Summary and discussion of this scenario is given in Sect. 8.

54
55

56 **2. Summary of onset timing study using ground Pi2s at the equator**

57 In this section, we summarize field line dipolarization occurring at the geosynchronous orbit
58 based on the statistical results obtained by Saka et al. [2010]. The authors used
59 magnetometer data from geosynchronous satellites (Goes5 and Goes6) and those at ground
60 equatorial stations (Huancayo, Peru, $1.4^\circ N$ in geomagnetic latitudes) in the conjugate
61 meridian. Goes5 was located at higher latitudes, $10.3^\circ N$ in dipole coordinates, and Goes6
62 was closer to the equator; $7.9^\circ N$ in dipole coordinates. This difference was caused by the
63 separated meridians of the satellites (2.2 hours of local time). The dipole coordinate used are
64 equivalent to the HDV coordinates; H is positive northward along the dipole axis, V is radial
65 outward, and D denotes dipole east. The field line dipolarization at the geosynchronous orbit
66 can be characterized either by a step-like or impulsive increase of inclination angle of the
67 geomagnetic field lines. The inclination angle is measured positive northward from the dipole
68 equator. The step-like dipolarization was observed by Goes5 located at higher latitudes, while
69 the dipolarization pulse was observed by Goes6 at latitudes closer to the equatorial plane.
70 The onset of field line dipolarization preceded the initial peak of the ground Pi2 pulse by two
71 minutes, suggesting that the onset was initiated in association with the first increase of the
72 Pi2 amplitudes. Following the dipolarization onset, field line magnitude decreased at the

73 geosynchronous orbit, and field lines deflected westward in the dawn sector and eastward in
 74 the dusk sector (see Figure 1 for dawn-dusk deflection, reproduced from [Saka et al., 2010]).
 75 This is caused by the dawn-dusk expansion of the plasma flows occurring tailward of the
 76 geosynchronous orbit. These longitudinal expansions lasted for about 10 min and decreased
 77 the field magnitudes therein. Expansion in the dusk sector, however, continued over this
 78 characteristic 10-min-interval. Asymmetries of the dawn-dusk expansion may be caused by
 79 diamagnetic drifts in the plasma sheet [Liu et al., 2013]. It is suggested that classical
 80 dipolarization, caused by the reduction of cross-tail currents in the midnight magnetosphere,
 81 happened after the nightside magnetosphere experienced this characteristic 10-min-interval.
 82 For this reason, the first 10 min intervals are referred to as transitional state of substorm
 83 expansion [Saka et al., 2010].

84
 85

86 **3. Pre-onset intervals leading to field line dipolarization**

87 In the pre-onset intervals, decrease of the field line inclination started two hours prior to the
 88 dipolarization onset. It attained minimum angles (33.6° for Goes5 and 49.4° for Goes6 in
 89 dipole coordinates) right before the dipolarization onset [Saka, 2010; 2019].

90 One of the properties of plasmas in pre-onset intervals are continuing inflows of lobe plasmas
 91 towards the equatorial plane [Birn and Hesse, 1996], Poynting flux enhancement [Machida
 92 et al., 2009], and Ey (westward electric fields) penetration toward the equatorial plane
 93 [Machida et al, 2014]. Corresponding plasma properties at geosynchronous altitudes may be
 94 predominant perpendicular temperature anisotropies of thermal plasmas (30eV - 40keV)
 95 obtained from three-dimensional temperature matrix and their gradual decrease towards the
 96 onset [Birn et al., 1997]. At the onset, however, increase of parallel anisotropy stopped and
 97 perpendicular anisotropy increased again. Such changes of temperature anisotropy at onset
 98 were observed in roll-angle spectrogram of energy flux of electrons in 15eV-40keV [Saka and
 99 Hayashi, 2017]. This transition of the temperature anisotropies may be accounted for by the
 100 following scenario.

101 A continuing tailward stretch of the field lines in the pre-onset intervals as depicted in Figure
 102 2 may increase equatorward flux by the counterclockwise rotation of the inflow vectors (F_{\perp})
 103 in the north of the equatorial plane (clockwise rotation in the south) and produce a parallel
 104 component as well by the relation,

$$105 \quad \delta F_{\parallel} = F_{\perp} (\omega \cdot \delta t) \quad (1)$$

106 Here, δF_{\parallel} denotes increase of parallel flux per time, δt , ω is angular velocity of rotation
 107 of F_{\perp} vectors associated with the thinning of the flux tubes caused by stretching. In pre-
 108 onset intervals lasting 90 min at geosynchronous altitudes, field line stretching decreased the
 109 field line inclination by 7° from 40.6° to 33.6° [Saka, 2019]. This gives angular velocity
 110 of rotation of field line inclination in equation (1) as $1.4 \times 10^{-3} \text{ rad} / \text{min}$. Total parallel flux
 111 gained in T min may be given by the integral of equation (1) with time from 0 to T. Substituting
 112 T=60 min and $1.4 \times 10^{-3} \text{ rad} / \text{min}$ for angular velocity of field line inclination, this yields
 113 $F_{\parallel} = 8.2 \times 10^{-2} \cdot F_{\perp}$. Gain of F_{\parallel} is about 10% of the perpendicular flux (F_{\perp}). This is
 114 consistent with the parallel temperature anisotropies gained prior to the onset (20% gain) in
 115 geosynchronous orbit [Birn et al., 1997].
 116 Continuing parallel flux flows associated with the flux tube stretching in the pre-onset intervals
 117 may increase plasma pressures in the flux tube at its tailward end. This condition leads to
 118 further stretching of the flux tube (small curvature radius) [Ohtani and Tamao, 1993; Rubtsov
 119 et al., 2018] by the relation,

$$120 \quad \frac{\beta}{2} \kappa + \kappa_B + \frac{1}{R} = 0 \quad (2)$$

121 Here, β is plasma to magnetic pressure ratio, κ and κ_B denote reciprocal spatial scales
 122 of radial inhomogeneity of plasma pressure and magnetic fields in the equatorial plane,
 123 respectively. R is curvature radius of the field lines.

124
 125

126 **4. Excitation of slow magnetoacoustic wave**

127 The continuing parallel flows may excite magnetoacoustic wave. From a set of linearized
 128 MHD equations we have relation between parallel displacement along the field lines (ξ_z)
 129 and divergence of perpendicular displacements (ξ_{\perp}) in the following form (see Appendix),

$$130 \quad \xi_z = \frac{C_s^2}{\omega^2} F \cdot B_0^2 \frac{\partial}{\partial z} (\text{div} \xi_{\perp}) \quad (3)$$

131 Here, C_s , ω and B_0 are the sound velocity, angular frequency of waves and background
 132 field magnitudes, respectively. F is given by

133

$$F = \frac{C_A^2}{B_0^2} \frac{1}{C_s^2 - \left(\frac{\omega}{k}\right)^2} \quad (4)$$

134

135

136

137

138

139

140

141

142

143

144

145

146

147

148

149

150

151

152

153

154

155

156

157

158

159

160

161

162

163

164

165

F is positive for the slow magnetoacoustic wave and negative for the fast magnetoacoustic wave. C_A and k denote Alfvén velocity and wave vector, respectively. We use equation (3) for the classification of slow and fast magnetoacoustic waves. Slow magnetoacoustic wave yields perpendicular expansion of the flux tubes at the converging point of parallel flows on the equatorial plane. For fast wave, perpendicular shrinkage of flux tubes occurs at the converging point of parallel flows (equatorial plane).

The equation (3) will be applied to simulate possible effect of magnetoacoustic wave on pitch angle spectrogram. For this, we used drift Maxwell distributions for phase space density (PSD) assuming gyrotropy for particle trajectories. PSD was composed of three parts: one drifting parallel, another anti-parallel along the field lines, and the third part perpendicular to the field lines. Figure 3(A) shows pitch angle spectrogram of energy flux with no drift velocities either perpendicular or parallel to the background field lines. Energy flux is defined by

$(2E^2/m^2)f$, where E , m , f are energy, mass of particles, and phase space density,

respectively. Energy flux is given in $eV / (cm^2 s \cdot sr \cdot eV)$. Only parallel drift increased in from $0.3V_{th}$, $0.6V_{th}$, and to $1.0V_{th}$ as shown in B, C, and D. For E and F, perpendicular drift increased to $0.3V_{th}$ and $0.5V_{th}$ while parallel drift remained at $1.0V_{th}$. Energy fluxes initially in quasi-trapped distribution (A) changed to more parallel and anti-parallel fluxes as parallel and anti-parallel drift increased (B, C, and D). Increasing perpendicular drifts increased perpendicular fluxes in the pitch angle distributions of E and F.

We clarified that magnetoacoustic wave produced coupling of parallel flux along the field lines and the perpendicular flux. However, we choose slow magnetoacoustic wave for the wave mode because the flux tubes expanded (did not shrink) in the transitional interval as discussed in Section 2. Slow magnetoacoustic wave may be triggered through Ballooning instability, when enough pressure gradient is accomplished in an earthward direction [Ohtani and Tamao, 1989; Rubtsov et al., 2018].

We can estimate the Ballooning instability threshold κ (reciprocal scale of radial inhomogeneity of plasma pressure) using calculation results given in [Rubtsov et al., 2018].

In a distance from $L=5$ to $10R_e$, instability threshold is given approximately as $\kappa = -1.0R_e^{-1}$ (κ denotes reciprocal spatial scale of radial inhomogeneity of plasma pressure, and R_e is the Earth radius) for beta defined by the ratio of plasma pressure and magnetic pressure exceeding 0.1. This suggests that the Ballooning instability develops at the geosynchronous altitudes (curvature radius R is $2.2R_e$) when spatial scale of the earthward pressure gradient

166 caused by the inflows becomes steeper than 1.0 Re. We show in the following section that
167 this theoretical consideration matched observations.

168

169

170 **5. Field line dipolarization in the vicinity of geosynchronous orbit**

171 **5.1 Relaxation of radial inhomogeneity**

172 We can assume the westward electric fields in Dipolarization Front (DF) [Runov et al., 2011]
173 embedded in the leading edge of Bursty Bulk Flow (BBF) as external stimulus for triggering
174 Ballooning instability. In this case westward electric fields in the DF temporarily amplified the
175 parallel flux flowing towards the end point of the flux tube in the equatorial plane and further
176 steepen earthward pressure gradient. If it exceeds instability threshold determined by β
177 and initial curvature radius R , slow magnetoacoustic wave can be excited [Rubtsov et al.,
178 2018]. Once the slow magnetoacoustic wave was excited, perpendicular fluxes spread the
179 plasmas in dawn-dusk directions and smooth (or relax) the radial gradient of plasma
180 pressures in the equatorial plane (smaller κ). This may result in the transition of the flux
181 tube geometry to a new configuration, an increase of the curvature radius of the field lines
182 (larger R) (see equation (2)).

183 We revisit multiple Pi2 events observed by AMPTE CCE on 31 August 1986 [Saka et al.,
184 2002] and show an example of relaxation of radial inhomogeneity of plasma pressures
185 associated with field line dipolarization in Figure 4. The satellite passed the midnight sector
186 (20 – 23 MLT) from 3 Re to 7 Re at latitudes south of the equatorial plane (-8° MLat) when
187 multiple Pi2 event (with positive bay) were observed at low latitude station (KUJ) at L=1.2 in
188 the midnight sector (Figure 4A). Inclination angle of field lines along the satellite trajectory is
189 shown in Figure 4(B). Dipolarization occurred as marked by vertical arrows correlating to

190 multiple onset of Pi2s, 1 through 4 in Figure 4(A). Ion fluxes coming from dawn sector (\mathbf{J}_-)

191 and from dusk sector (\mathbf{J}_+) at satellite altitudes were measured by the instruments (two

192 energy channels, 63-85 keV and 125-210 keV) on board AMPTE CCE [Takahashi et al.,
193 1996]. A schematic of particle measurement is shown at the top of Figure 5. The flux

194 difference ($\mathbf{J}_- - \mathbf{J}_+ > 0$) increased in association with the onset of multiple Pi2 (15:05 UT)

195 and positive bay at KUJ (Figures 4C and 4D). Sudden increase was followed by the slow
196 decrease of flux in 63-85 keV channel and rapid decrease of flux in 125-210 keV channel.

197 The flux difference, $\mathbf{J}_- > \mathbf{J}_+$, may be caused either by earthward pressure gradient or

198 westward convection of plasmas. From the different patterns of the flux decrease with time
199 in two energy channels, we can suggest that the measured flux difference, $\mathbf{J}_- - \mathbf{J}_+$, can be
200 attributed to increase of the earthward pressure gradient and succeeding relaxation. Note
201 that guiding center of $\mathbf{J}_- / \mathbf{J}_+$ is earthward/tailward of the satellite position as depicted in
202 top of Figure 5. The different relaxation speed in two energy channels, slower for 63-85 keV
203 and faster for 125-210 keV, suggest that the earthward pressure gradient (assumed to be
204 proportional to the flux gradient) decreased with time during the multiple Pi2 event (Figure 5).
205 The flux difference (50 counts/sample) was 10% of the background flux both for 63-85 keV
206 (Larmor radius is 250 km for 150 nT) and for 125-210 keV (Larmor radius is 450 km), that is,
207 the flux level differed by 10% at two locations 1000 km apart in radial distance for 63-85 keV
208 and 1800 km for 125-210 keV. This gives e-folding scale of the earthward pressure gradient
209 being 0.98 Re and 1.77 Re for 63-85 keV and 125-210 keV, respectively. The 31 August
210 event shows that radial pressure gradient was relaxed in the inner magnetosphere in
211 association with the increase of the field line inclination (dipolarization). Although the field line
212 dipolarization showed a sharp onset in satellite magnetometer data, we note that it did not
213 occur in ion flux data. This may be true because the ion flux change at the onset may be
214 obscured by the contamination from the past onsets transported across the field lines from
215 the adjoining sector by the electric fields and gradient/curvature drifts. We conclude that the
216 relaxation of spatial inhomogeneity started when the spatial scale of the radial inhomogeneity
217 approached 1.0 Re, consistent with theoretical consideration of Ballooning instability by
218 Rubtsov et al (2018).

219

220 **5.2 Flux tube transition to a new geometry**

221 Meanwhile, field lines in the further earthward locations may be compressed by the inward
222 movement of the outer field lines. This process associated with the dipolarization onset may
223 increase the parameter κ_B in equation (2) which may result in transition to a new geometry
224 of earthward field lines, a decrease of the curvature radius R . Transition of the field line
225 geometries for onset locations and ones in earthward locations are schematically illustrated
226 in Figure 6. These field line geometries in meridian plane matched the third harmonic and
227 fundamental harmonic deformations of outer and inner field lines, respectively. This is often
228 observed in the midnight magnetosphere in the initial pulse of Pi2s [Saka et al., 2012].
229 Transitions of the flux tube geometry in magnetosphere also correspond to the production of
230 negative bay in higher latitudes and positive bay in lower latitudes. If we can assume that
231 negative bay switched to positive bay at latitudes, 60 degrees in geomagnetic coordinates

232 for examples, this latitude can be mapped beyond the geosynchronous orbit ($L \sim 7 R_E$ or
233 further tailward) as field line dipolarization occurs along the stretched flux tubes.
234 Consequently, this scenario requires that the BBFs are not necessary to reach inner
235 magnetosphere to trigger the substorm onset at lower latitudes. In the inset, flux tube
236 deformations are illustrated in the equatorial cross section at onset locations (field lines 1
237 and 2). Divergence of perpendicular flows (solid arrows) produced dawn-dusk expansion of
238 flux tube (2) and the shrinkage of stretched flux tube (1) by relaxation of the radial
239 inhomogeneity. Flux tube deformation from 1 to 2 tended to preserve the total magnetic fluxes
240 in the equatorial cross section. From the local time distribution of the dawn-dusk expansion
241 of the flux tubes shown in Figure 1, most of the flux tube transition such as from 1 to 2 may
242 occur tailward of geosynchronous orbit. Some of the events, however, may happen
243 earthward of the geosynchronous orbit [i.e., Ohtani et al., 2018].

244 Increasing of the curvature radius, or earthward shrinkage of the flux tubes, produce a
245 reduction of the radial component of the field lines (V in dipole coordinates) by adding positive
246 V in the north of the equatorial plane and negative V in the south. If amplitudes of the V
247 component changed by 10 nT in one minute, the expected inductive electric fields (westward)
248 could be of the order of 1.0 mV/m when shrinkage was confined within 1 R_E from the
249 equatorial plane. The dawn-dusk expansion of the flux tubes may also produce inductive
250 electric fields (earthward and tailward in dawn and dusk sector, respectively) of the same
251 order of magnitudes. They are Alfvén waves, a wave mode in Ballooning instability coupled
252 with slow magnetoacoustic wave [Rubtsov et al., 2018]. The westward electric fields produce
253 earthward flow bursts referred to as convection surge. The inductive electric fields produced
254 by the dipolarization are the same order of magnitudes observed in DF [Runov et al., 2011].

255

256

257 **6. Coupling of magnetosphere and ionosphere in association with field line** 258 **dipolarization**

259 The inductive electric fields may be transmitted along the field lines as poloidally and
260 toroidally polarized Alfvén waves [Klimushkin et al., 2004]. These electric fields produce a
261 dynamic ionosphere in polar region that includes nonlinear evolution of ionospheric plasmas
262 (poleward expansion), as well as production of field-aligned currents and parallel potentials
263 by exciting ion acoustic wave in quasi-neutral condition [Saka, 2019]. It is not the aim of this
264 paper to describe in detail the dynamic processes in the ionosphere, but to show a local
265 production of currents in the ionosphere as well as field-aligned currents by the penetrated
266 electric fields. For this purpose, we revisit the 10 August 1994 substorm event studied by
267 Saka and Hayashi (2017). In this event, eastward expansion was observed of the field line

268 dipolarization region, started at 11:55 UT (00:27 MLT) from 260 ° E of geomagnetic longitudes
 269 and expanded to 351 ° E in about 48 min. At the leading edge of the expansion, ground
 270 magnetometer data showed bipolar event (quick change of the D component from positive
 271 to negative in about 5 min), being confined in the expanding dipolarization front as a
 272 substructure. The substructure in the leading edge of the field line dipolarization will be
 273 examined as follows.

274 We can assume that magnetic signals on the ground are associated with the sum of the
 275 horizontal Hall currents in the ionosphere [Fukushima, 1971]. These currents can be
 276 calculated by the relation,

$$277 \quad (\text{rot } \mathbf{J})_z = -\frac{1}{\mu_0} \nabla^2 B_z \quad (5)$$

278 We used the ground vertical component (b) as a proxy of B_z in the ionosphere. The second
 279 derivative in right-hand side of equation (5) is approximated as,

$$280 \quad \nabla^2 B_z^i = \left(\frac{b^{i+1} - b^i}{L_{i+1} - L_i} - \frac{b^i - b^{i-1}}{L_i - L_{i-1}} \right) / (L_{i+1} - L_{i-1}) \quad (6)$$

281 Here, i denotes i -th station in the meridian chain. L_i is the geomagnetic latitude of the i -th
 282 station. We considered meridional change only. This is because the vertical component
 283 changed from negative to positive across the meridian, while in longitudes it changed simply
 284 decreasing or increasing in lower and higher latitudes after onset, respectively. Hence,
 285 longitudinal variations may contribute less to the Laplacian. The results reproduced from
 286 Saka and Hayashi (2017) are shown in Figure 7(A). The eastward propagation of
 287 dipolarization front crossed this meridian (300 ° E) at 12:13 UT corresponding to the interval
 288 labelled 1. Two points arose from this figure; (1) Loop of Hall current pair existed, CCW
 289 viewed from above the ionosphere in the lower latitudes and CW in the higher latitudes, (2)
 290 These current patterns expand poleward. Current patterns in the interval from 1 to 5 in Figure
 291 7(A) are illustrated in Figure 7(B) to facilitate the poleward expansion. It is clearly
 292 demonstrated that current pair forming CW in higher latitudes and CCW in lower latitudes
 293 expanded in time towards the pole. Bipolar change can be recorded in the D component data
 294 (not shown) when the ground station, FSIM in this case, passes from segment 1 to 2 in Figure
 295 7(B). As a result, dipolarization front expanded eastward progressively by producing the
 296 poleward expansion at each meridian. The front left behind the current pattern comprising
 297 upward field-aligned currents in lower latitudes and downward in higher latitudes, or Bostrom
 298 type current system. We propose that the ionosphere itself has inherent electromotive force
 299 to drive this Bostrom type current system. The reasons are as follows.

300 In the E region, drift trajectories may be written [Kelley, 1989] for electrons by,

301
$$\mathbf{U}_{e\perp} = \frac{1}{B}[\mathbf{E} \times \hat{\mathbf{B}}] \quad (7)$$

302 and for ions by,

303
$$\mathbf{U}_{i\perp} = b_i[\mathbf{E} + \kappa_i \mathbf{E} \times \hat{\mathbf{B}}]. \quad (8)$$

304 Here, b_i is mobility of ions defined as $\Omega_i/(B\nu_{in})$, κ_i is defined as Ω_i/ν_{in} . Symbols Ω_i
 305 and ν_{in} are ion gyrofrequency and ion-neutral collision frequency, respectively. $\hat{\mathbf{B}}$ denotes
 306 a unit vector of the magnetic fields B . We assumed that $\mathbf{E} \times \mathbf{B}$ drifts for electrons and
 307 ions were driven by westward electric fields transmitted from the convection surge. Because
 308 of very low mobility of ions in E layer ($\kappa_i = 0.1$), electric field drifts accumulate electrons (not
 309 ions) in lower latitudes and produce stronger secondary southward electric fields in the
 310 ionosphere. The southward electric fields produced southward motion of ions due to the first
 311 term of equation (8). They carry Pedersen currents (ion currents) for producing quasi-
 312 neutrality of ionosphere. $\mathbf{E}_w \times \mathbf{B}$ drifts caused by the transmitted westward electric fields
 313 (\mathbf{E}_w) may propel electrons against southward electric fields from higher latitudes to lower
 314 latitudes as electromotive force to maintain the potential drop for driving Pedersen currents.
 315 This means the ionospheric E layer contains both generator and load in it. In quasi-neutral
 316 condition, a small imbalance of particle densities of electrons and ions ($n_e - n_i \sim 10^2 m^{-3}$)
 317 may induce in lower latitudes negative potential region of the order of -100 kV with horizontal
 318 scale length of 100 km. To sustain this negative potential, upward field-aligned currents of
 319 the order of $1.0 \mu A / m^2$ for $\Sigma_p \sim 10^0 S$ must flow. Downward field-aligned currents from
 320 the positive potential regions in the higher latitudes may also be expected. It is supposed that
 321 upward field-aligned currents may be carried mostly by ions flowing outwards and downward
 322 currents are escaping electrons to the magnetosphere. Those ions and electrons escape
 323 from the ionosphere into the magnetosphere to assure quasi-neutral conditions of the
 324 ionosphere. The above scenario may be adapted to a creation of the incomplete Cowling
 325 channel [Baumjohann, 1983], where unbalanced primary northward Hall currents and
 326 secondary southward Pedersen currents driven by the polarization electric fields yielded
 327 field-aligned currents.

328

329

330 **7. Triggering mechanisms of low latitude Pi2s**

331 From ground magnetometer observations in auroral zone, it is natural to assume that flux
332 tubes linked to negative bay (decreasing of the H component) and positive bay (increasing
333 of the H component) at higher and lower latitudes, respectively, oscillated coherently at Pi2
334 periods. Oscillating flux tubes associated with positive bay may produce local compression
335 of magnetic fields in the equator and trigger cavity mode in low latitudes [Takahashi et al.,
336 1995]. Oscillations, however, are short-lived and may not establish true cavity modes. They
337 excite cavity/waveguide modes in the plasmasphere [Allan et al., 1996; Li et al., 1998].

338 In the dip-equator, a singular latitude of the cavity/waveguide mode, only isotropic mode can
339 be excited [Allan et al., 1996]. This leads us to suppose that a very large propagation velocity
340 (or large wavelength exceeding whole circle of the Earth) of equatorial Pi2s in the nightside
341 sector [Kitamura et al., 1988] would be associated with the dawn-dusk asymmetries of non-
342 propagating compressions.

343 Pi2 periodicity may be determined primary by consecutive arrival of BBF substructures
344 referred to as dipolarization front bundle (DFB) [Liu et al., 2013, 2014]. Repeating arrival of
345 DFB produces periodic dipolarization or oscillation of negative bays. Positive bay oscillations
346 in the plasmasphere would follow the negative bay oscillations to excite cavity/waveguide
347 modes for low to equatorial Pi2s at the same periodicities. To estimate the onset time of the
348 field line dipolarization using the very low latitudes Pi2s, delays in transmission are from the
349 magnetosphere; longitudinal delays across the meridian may not be significant.

350 High latitude Pi2s may not be caused by cavity/waveguide modes but by oscillation of field-
351 aligned currents comprising Bostrom type current system (incomplete Cowling channel), R1
352 (region 1) type current system associated with convection surge [i.e., Birn and Hesse, 1996],
353 and R2 (region 2) type current system of expanding flux tubes in longitudes [i.e., Tanaka et
354 al., 2010]. In contrast to the very-low latitude Pi2s associated with the non-propagating
355 compression, the high-latitude Pi2s propagated on the ground typically at 20km/s eastward
356 and westward in the sector east and west of the substorm center, respectively [Samson and
357 Harrold, 1985]. Propagation across the meridian may cause further delays, 35 sec for
358 propagation of 1 hour of local time. We should exercise caution when using high latitude Pi2s
359 for timing study.

360 The above scenario assumes that the DFBs arrived periodically in the inner magnetosphere
361 at a frequency not very different than the cavity frequency of plasmasphere.

362

363

364 **8. Discussion and Summary**

365 Definition of field line dipolarization is a configuration change from stretching to shrinkage of
366 geomagnetic field lines in the midnight meridian of magnetosphere. Two models have been
367 proposed to account for the configuration change; diversion of the cross-tail currents via
368 ionosphere, referred to as substorm current wedge (SCW), as first proposed in McPherron
369 et al. [1973] and extinction of the cross-tail currents by a local kinetic instability, current
370 disruption (CD) [Lui, 1996]. These models have been adopted for many decades to account
371 for the critical issues associated with substorm onset. We propose, based on Ballooning
372 instability scenario, that field line dipolarization is caused by the relaxation of radial
373 inhomogeneity of plasma pressures in association with the excitation of slow
374 magnetoacoustic wave. Dipolarization regions expand in longitudes and decrease field
375 magnitudes by expanding flux tubes therein. This condition continued for about 10 min and
376 classical dipolarization caused by the reduction of cross-tail currents or pileup of the magnetic
377 flux transported from the tail begins.

378 **It is noted that BBFs with low entropy plasmas (plasma bubbles) often penetrated to**
379 **the inner magnetosphere [Dubyagin et al., 2011]. In numerical simulations, those**
380 **bubbles localized in local time produced global dipolarization in the inner**
381 **magnetosphere [Merkin et al., 2019] and generated ionospheric current system such**
382 **as westward electrojet, Harang discontinuity, and poleward expansion of aurora in**
383 **substorm expansion phase [Yang et al., 2012]. These classical features of substorm**
384 **expansion occurred in this first 10 min intervals of Pi2 onset referred to as transitional**
385 **intervals in the midnight magnetosphere. The transitional intervals may be the most**
386 **active periods in the substorm phase.**

387 The proposed scenario was deduced from the geosynchronous observation and cannot be
388 readily applied to the onset scenario beyond the geosynchronous orbit. Nevertheless, dawn-
389 dusk expansion of the flux tubes may be a fundamental property of field line dipolarization
390 not only at geosynchronous altitudes but also in tailward locations (8 - 12 Re) [Yao et al.,
391 2013; Liu et al., 2013]. It is suggested that the field line dipolarization at tailward locations is
392 subdivided by faster expanding (in longitudes) dipolarization front (DF) and slower expanding
393 dipolarization front bundle (DFB) led by DF [Liu et al., 2015]. Such substructures in field line
394 dipolarization are also observed at geosynchronous altitudes [Saka and Hayashi, 2017]. The
395 geosynchronous dipolarization expanded (in longitudes) at 1.9 km/s, while Pi2s emitted in
396 the dipolarization region propagated one order of magnitude faster. The fast longitudinal
397 velocities associated with Pi2s may be embedded within the slowly expanding region of
398 dipolarization, similarly to the relationship between DF and DFB. If this relationship can be
399 adapted also to the transitional state and succeeding field line pileup, the dipolarization

400 scenario at geosynchronous observations can be extended further tailward in upstream. Or,
401 the onset scenario in 10 Re can be applied in geosynchronous dipolarization. In that case,
402 dipolarization pulse at Goes6 latitudes ($7.9^{\circ} N$) may represents DFs. This assumption may
403 be supported because electron energy flux pitch angle distributions in tailward locations
404 beyond 10Re show parallel to perpendicular transitions, like ones in Figure 3, at the arrival
405 of DF [Deng et al., 2010].

406 We emphasize that two different types of the dipolarization exist in the substorms; one is
407 associated with change of curvature radius of field lines in the transitional state (faster
408 expansion in longitudes) and the other is subsequent pileup of the magnetic flux transported
409 from the tail (slower expansion). **Field line pileup caused by the flow braking processes**
410 **[Shiokawa et al., 1997] may lead to tailward regression of the dipolarization region as**
411 **reported in Baumjohann et al. [1999].**

412 In the transitional state lasting for about 10 min, the inductive electric fields pointing westward
413 were produced in the equatorial plane. They propagated along the field lines to the
414 ionosphere to produce meridional field-aligned currents of the Bostrom type (downward in
415 higher latitudes and upward in lower latitudes). The Bostrom type current system was indeed
416 observed on the ground at the front of dipolarization expanding towards east. The
417 magnetospheric dynamo produced by earthward electric fields in the equatorial plane
418 [Akasofu, 2003] and the E layer dynamo in the ionosphere worked together to activate the
419 Bostrom current system.

420
421

422 **9. Code/Data availability**

423 **Satellite data from Goes5/6, AMPTE CCE and ground magnetometer data in Figures 1,**
424 **4 and 7 is available upon request to Osuke Saka (saka.o@nifty.com).**

425

426 **10. Competing interest**

427 The author declares that there is no conflict of interest.

428
429

430 Acknowledgements

431 The author would like to express his sincere thanks to all the members of Global Aurora
432 Dynamics Campaign (GADC) [Oguti et al., 1988]. **We are also grateful to anonymous**
433 **referees for their critical review.**

434
435

436 Appendix

437 In order to derive equations (3) and (4), we first follow Kadomtsev (1979). Linearized MHD
438 equations may be written as,

$$439 \quad \frac{\partial^2 \boldsymbol{\xi}}{\partial t^2} = C_s^2 \nabla \operatorname{div} \boldsymbol{\xi} + C_A^2 \nabla_{\perp} \operatorname{div} \boldsymbol{\xi}_{\perp} + C_A^2 \frac{\partial^2 \boldsymbol{\xi}_{\perp}}{\partial z^2}. \quad (\text{A1})$$

440 Here, C_s , C_A , $\boldsymbol{\xi}$ denote sound velocity, Alfvén velocity, plasma displacement, respectively.
441 (\perp, z) denote perpendicular and parallel component with respect to the background field
442 lines.

443 After a few manipulations of (A1), we have magnetoacoustic wave equations for finite β
444 plasmas:

$$445 \quad \frac{\partial^2 \operatorname{div} \boldsymbol{\xi}_{\perp}}{\partial t^2} = C_A^2 \Delta \operatorname{div} \boldsymbol{\xi}_{\perp} + C_s^2 \Delta_{\perp} \operatorname{div} \boldsymbol{\xi} \quad (\text{A2})$$

446 and

$$447 \quad \frac{\partial^2 \xi_z}{\partial t^2} = C_s^2 \frac{\partial}{\partial z} (\operatorname{div} \boldsymbol{\xi}) \quad (\text{A3})$$

448 Equations (A2) and (A3) present compressive properties across and along the background
449 field lines, respectively.

450 Assuming plane harmonic wave solutions, first order quantities of density and magnetic field
451 compressions $(\delta n, \delta \mathbf{B})$ may be given by the following equation.

$$452 \quad \frac{\delta n}{n_0} = -\frac{C_A^2}{B_0^2} \frac{1}{C_s^2 - \left(\frac{\omega}{k}\right)^2} (\mathbf{B}_0 \cdot \delta \mathbf{B}) \quad (\text{A4})$$

453 Here, n_0 , B_0 denote background density and magnetic fields, respectively.

454 Substitution of (A4) into (A3) using $\operatorname{div} \boldsymbol{\xi} = -\delta n/n_0$ yields

$$455 \quad \frac{\partial^2 \xi_z}{\partial t^2} = C_s^2 F \frac{\partial}{\partial z} (\mathbf{B}_0 \cdot \delta \mathbf{B}). \quad (\text{A5})$$

$$456 \quad \text{Here, } F = \frac{C_A^2}{B_0^2} \frac{1}{C_s^2 - \left(\frac{\omega}{k}\right)^2}$$

457 Linearized Faraday's law in frozen-in condition, $\delta \mathbf{B} = \nabla \times (\boldsymbol{\xi}_{\perp} \times \mathbf{B}_0)$, may be reduced to

$$458 \quad \delta \mathbf{B} = -\mathbf{B}_0 \operatorname{div} \boldsymbol{\xi}_{\perp} + B_0 \frac{\partial}{\partial z} \boldsymbol{\xi}_{\perp}. \quad (\text{A6})$$

459 Substituting (A6) into (A5), we have final expressions relating parallel and perpendicular
460 displacements as,

461
$$\frac{\partial^2 \xi_z}{\partial t^2} = -C_s^2 F \cdot B_0^2 \frac{\partial}{\partial z} (\text{div} \xi_{\perp}). \quad (\text{A6})$$

462 Replacing $\partial/\partial t$ with $-i\omega$, (A6) yields the equation (3) in Section 4,

463
$$\xi_z = \frac{C_s^2}{\omega^2} F \cdot B_0^2 \frac{\partial}{\partial z} (\text{div} \xi_{\perp}).$$

464

465

466

467 **References**

468 Akasofu, S.-I.: Source of auroral electrons and the magnetospheric substorm current system,
469 J. Geophys. Res., 108, A4, 8006, doi:10.1029/2002JA009547, 2003.

470 Allan, W., F.W. Menk, B.J. Fraser, Y. Li, and S.P. White, Are low-latitude Pi2 pulsations
471 cavity/waveguide mode?, Geophys. Res. Lett., 23, 765, 1996.

472 Baumjohann, W.: Ionospheric and field-aligned current systems in the auroral zone: A
473 concise review, Adv. Space Res., 2, 55-62, 1983.

474 Baumjohann, W., Hesse, M., Kokubun, S., Mukai, T., Nagai, T., and Petrukovich, A.A.:
475 Substorm dipolarization and recovery, J. Geophys. Res., 104, 24995-25000, 1999.

476 Birn, J., and Hesse, M.: Details of current disruption and diversion in simulations of
477 magnetotail dynamics, J. Geophys. Res., 101, A7, 15345-15358, 1996.

478 Birn, J., Thomsen, M.F., Borovsky, J.E., Reeves, G.D., McComas, D.J., and Belian, R.D.:
479 Characteristic plasma properties during dispersionless substorm injections at
480 geosynchronous orbit, J. Geophys. Res., 102, A2, 2309-2324, 1997.

481 Deng, X, Ashour-Abdalla, M., Zhou, M., Walker, R., El-Alaoui, M., Angelopoulos, V., Ergun,
482 R.E., and Schriver, D.: Wave and particle characteristics of earthward electron
483 injections associated with dipolarization fronts, J. Geophys. Res., 115, A09225,
484 doi:10.1029/2009JA015107, 2010.

485 Dubyagin, S., Sergeev, V., Apatenkov, S., Angelopoulos, V., Runov, A., Nakamura, R.,
486 Baumjohann, W., McFadden, J., and Larson, D.: Can flow bursts penetrate into the
487 inner magnetosphere?, Geophys. Res. Lett., 38, L08102, doi:10.1029/2011GL047016,
488 2011.

489 Fairfield, D.H., Mukai, T., Brittnacher, M., Reeves, G.D., Kokubun, S., Parks, G.K., Nagai, T.,
490 Mtsumoto, H., Hashimoto, K., Gurnett, D.A., and Yamamoto, T.: Earthward flow bursts
491 in the inner magnetotail and their relation to auroral brightenings, AKR intensifications,
492 geosynchronous particle injections and magnetic activity, J. Geophys. Res., 104, A1,
493 355-370, 1999.

494 Fukushima, N.: Electric current systems for polar substorms and their magnetic effect below
495 and above the ionosphere, *Radio Sciences*, 6, 269-275, 1971.

496 Kadomtsev, B.B.: *Collective phenomena in plasmas* (in Japanese), Iwanami shoten, Tokyo,
497 1979. **(English edition published in 1982 is available from Pergamon Press)**

498 Kelley, M.C.: *The earth's ionosphere: plasma physics and electrodynamics*, Academic Press,
499 Inc, 1989.

500 Kitamura, T., Saka, O., Shimoizumu, M., Tachihara, H., Oguti, T., Araki, T., Sato, N., Ishitsuka,
501 M., Veliz, O., and Nyobe, J.B.: Global mode of Pi2 waves in the equatorial region:
502 Difference of Pi2 mode between high and equatorial latitudes, *J. Geomag. Geoelectr.*,
503 40, 621-634, 1988.

504 Klimushkin, D.Yu., Mager, P.N., and Glassmeier, K.-H.: Toroidal and Poloidal Alfvén waves
505 with arbitrary azimuthal wave numbers in a finite pressure plasma in the Earth's
506 magnetosphere, *Annales Geophysicae*, 22, 267-287, 2004.

507 Li, Y., B.J. Fraser, F.W. Menk, D.J. Webster, and K. Yumoto, Properties and sources of low
508 and very low latitude Pi2 pulsations, *J. Geophys. Res.*, 103, 2343, 1998.

509 Liu, J., Angelopoulos, V., Runov, A., and Zhou, X.-Z.: On the current sheets surrounding
510 dipolarizing flux bundles in the magnetotail: The case for wedgelets, *J. Geophys. Res.*,
511 118, 2000-20120, doi:10.1002/jgra50092, 2013.

512 Liu, J., Angelopoulos, V., Zhou, X.-Z., and Runov, A.: Magnetic flux transport by dipolarizing
513 flux bundles, *J. Geophys. Res.*, 119, 909-926, doi:10.1002/2013JA019395, 2014.

514 Liu, J., Angelopoulos, V., Zhou, X.-Z., Yao, Z.-H., and Runov, A.: Cross-tail expansion of
515 dipolarizing flux bundles, *J. Geophys. Res.*, 120, 2516-2530,
516 doi:10.1002/2015JA020997, 2015.

517 Lui, A.T.Y.: Current disruption in the Earth's magnetosphere: Observations and models, *J.*
518 *Geophys. Res.*, 101, 13067-13088, 1996.

519 Machida, S., Miyashita, Y., Ieda, A., Nose, M., Nagata, D., Liou, K., Obara, T., Nishida, A.,
520 Saito, Y., and Mukai, T.: Statistical visualization of the Earth's magnetotail based on
521 Geotail data and the implied substorm model, *Ann. Geophys.*, 27, 1035-1046, 2009.

522 Machida, S., Miyashita, Y., Ieda, A., Nose, M., Angelopoulos, V., and McFadden, J.P.:
523 Statistical visualization of the Earth's magnetotail and the implied mechanism of
524 substorm triggering based on superposed-epoch analysis of THEMIS data, *Ann.*
525 *Geophys.*, 32, 99-111, 2014.

526 McPherron, R.L., Russell, C.T., and Aubry, M.P.: Satellite studies of magnetospheric
527 substorms on August 15, 1968: 9. Phenomenological model for substorms, *J.*
528 *Geophys. Res.*, 78, 3131-3148, 1973.

529 Merkin, V.G., Panov, E.V., Sorathia, K.A., and Ukhorskiy, A.Y.: Contribution of bursty bulk

530 flows to the global dipolarization of the magnetotail during an isolated substorm,
531 J.Geophys.Res., 124, 8647-8668, <https://doi.org/10.1029/2019JA026872>.

532 Miyashita, Y., Machida, S., Kamide, Y., Nagata, D., Liou, K., Fujimoto, M., Ieda, A., Saito,
533 M.H., Russell, C.T., Christon, S.P., Nose, M., Frey, H.U., Shinohara, I., Muaki, T., Saito,
534 Y., and Hayakawa, H.: A state-of-the-art picture of substorm-associated evolution of
535 the near-Earth magnetotail obtained from superposed epoch analysis, J. Geophys.
536 Res., 114, A01211, doi:10.1029/2008JA013225, 2009.

537 Morioka, A., Miyoshi, Y., Miyashita, Kasaba, Y., Misawa, H., Tsuchiya, F., Kataoka, R.,
538 Kadokura, A., Mukai, T., Yumoto, K., Menietti, D.J., Parks, G., Liou, K., Honary, and
539 Donovan, E.: Two-step evolution of auroral acceleration at substorm onset, J.
540 Geophys. Res., 115, A11213, doi:10.1029/2010JA015361, 2010.

541 Nagai, T., Fujimoto, M., Saito, Y., Machida, S., Terasawa, T., Nakamura, R., Yamamoto, T.,
542 Mukai, T., Nishida, A., and Kokubun, S.: Structure and dynamics of magnetic
543 reconnection for substorm onsets with Geotail observations, J. Geophys. Res., 103,
544 A3, 4419-4440, 1998.

545 Nakamura, R., Baumjohann, W., Brittnacher, M., Sergeev, V.A., Kubyshkina, Mukai, T., and
546 Liou, K.: Flow bursts and auroral activations: Onset timing and foot point location, J.
547 Geophys. Res., 106, A6, 10777-10789, 2001.

548 Oguti, T., Kitamura, T., and Watanabe, T.: Global aurora dynamics campaign, 1985-1986, J.
549 Geomag. Geoelectr, 40, 485-504, 1988.

550 Ohtani, S.-I., Miura, A., and Tamao, T.: Coupling between Alfvén and slow magnetosonic
551 waves in an inhomogeneous finite- β plasma: 1 Coupled equations and physical
552 mechanism, Planet. Space Sci., 37, 567-577, 1989.

553 Ohtani, S.-I., and Tamao, T.: Does the ballooning instability trigger substorms in the near-
554 earth magnetotail?, J. Geophys. Res., 98, A11, 19369-19379, 1993.

555 Ohtani, S.-I., Motoba, T., Gkioulidou, M., Takahashi, K., and Singer, H.J.: Spatial development
556 of the dipolarization region in the inner magnetosphere, J.Geophys.Res., 123, 5452-
557 5463, doi.org/10.1029/2018JA025443.

558 Rubtsov, A.V., Mager, P.N., and Klimushkin, D.Yu.: Ballooning instability of azimuthally small
559 scale coupled Alfvén and slow magnetoacoustic modes in two-dimensionally
560 inhomogeneous magnetospheric plasma, Physics of Plasmas 25, 102903,
561 doi:10.1063/1.5051474, 2018.

562 Runov, A., Angelopoulos, V., Zhou, X.-Z., Zhang, X.-J., Li, S., Plaschke, F., and Bonnell, J.:
563 A THEMIS multicase study of dipolarization fronts in the magnetotail plasma sheet,
564 116, A05216, doi:10.1029/2010JA016316, 2011.

565 Saka, O., Akaki, H., and Baker, D.N.: A satellite magnetometer observation of dusk-to-dawn

566 current in the midnight magnetosphere at low-latitude Pi2 onset, *Earth Planets Space*,
567 54, e1-e4, 2002

568 Saka, O., Hayashi, K, and Thomsen, M.: First 10 min intervals of Pi2 onset at
569 geosynchronous altitudes during the expansion of energetic ion regions in the
570 nighttime sector, *J. Atmos. Solar Terr. Phys.*, 72, 1100-1109, 2010.

571 Saka, O., Hayashi, K., and Koga, D.: Excitation of the third harmonic mode in meridian planes
572 for Pi2 in the auroral zone, *J. Geophys. Res.*, 117, A12215,
573 doi:10.1029/2012JA018003, 2012.

574 Saka, O., and Hayashi, K.: Longitudinal expansion of field line dipolarization, *J. Atmos. Solar*
575 *Terr. Phys.*, 164, 235-242, 2017.

576 Saka, O.: A new scenario applying traffic flow analogy to poleward expansion of auroras, *Ann.*
577 *Geophys.*, 37, 381-387, 2019.

578 Sakurai, T., and Saito, T.: Magnetic pulsation Pi2 and substorm onset, *Planet. Space Sci.*, 24,
579 573-575, 1972.

580 Samson, J.C., and B.G. Harrold, Characteristic time constant and velocities of high-latitude
581 Pi2's, *J. Geophys. Res.*, 90, 12173, 1985.

582 Shiokawa, K., Baumjohann, W., and Haerendel, G.: Braking of high-speed flows in the near-
583 Earth tail, *J. Geophys. Res.*, 24, 10, 1179-1182, 1997.

584 Takahashi, K., Ohtani, S.-I., and Anderson, B.J.: Statistical analysis of Pi2 pulsations
585 observed by the AMPTE CCE spacecraft in the inner magnetosphere, *J. Geophys. Res.*,
586 100, A11, 21929-21941, 1995.

587 Takahashi, K., Anderson, B.J., and Ohtani, S.-I.: Multisatellite study of nightside transient
588 toroidal waves, *J. Geophys. Res.*, 101, A11, 24815-24825, 1996.

589 Tanaka, T., Nakamizo, A., Yoshikawa, A., Fujita, S., Shinagawa, H., Shimazu, H., Kikuchi, T.,
590 and Hashimoto, K.K.: Substorm convection and current system deduced from the
591 global simulation, *J. Geophys. Res.* 115, A05220, doi:10.1029/2009JA014676, 2010.

592 Yang, J., Toffoletto, F.R., Wolf, R.A., Sazykin, S., Ontiveros, P.A., and Weygand, J.M.: Large-
593 scale current systems and ground magnetic disturbance during deep substorm
594 injections, *J. Geophys. Res.*, 117, A04223, doi:10.1029/2011JA017415, 2012.

595 Yao, Z, Sun, W.J., Fu, S.Y., Pu, Z.Y., Liu, J., Angelopoulos, V., Zhang, X.-J., Chu, X.N., Shi,
596 Q.Q., Guo, R.L., and Zong, Q.-G.: Current structures associated with dipolarization
597 fronts, *J. Geophys. Res.*, 118, 6980-6985, doi:10.1002/2013JA019290, 2013.

598

599

600

601

602 Figure captions

603

604 Figure 1.

605 Upper panel: Local time distribution of W event and E event (see below). Lower panels:
606 Epoch superposition of field line deflections in degrees for Goes5/6. Those events with
607 eastward deflections (clockwise rotation, azimuth angle decreased) at T=0 shown to the left
608 (E event) and those with westward deflections (counterclockwise rotation, azimuth angle
609 increase) at T=0 are to the right (W event). T=0 marked by vertical dotted lines corresponds
610 to the first peak of the Pi2 waveform. Amplitudes at the onset (T=0) were subtracted from the
611 original data to adjust the pre-onset level. Plots covered 40 min from T-10 min to T+30 min.
612 Mean value of the epoch plot and mean value of band-passed (6-20 mHz: Pi2 band)
613 amplitudes are also shown. The field line rotations projected to the equatorial plane are
614 illustrated for E event and W event in the Figure (viewed from north of the equatorial plane).

615

616

617 Figure 2.

618 A progress of field line thinning in the growth phase is illustrated. The inflow flux (F_{\perp}) rotated
619 counterclockwise in times designated by red, green, and to blue arrows north of the
620 equatorial plane. South of the equatorial plane, rotation was in a clockwise direction. The
621 rotation of the inflow vectors produced the field-aligned component of the flux,
622 $\delta F_{\parallel} = F_{\perp}(\omega \cdot \delta t)$ as depicted in the inset with one in the northern hemisphere shown. Note
623 that inflows are localized earthward of the outer field lines.

624

625

626 Figure 3.

627 Simulated pitch angle spectrogram of energy flux for drift Maxwell distributions of phase
628 space density. Energy flux was shown in contour plots with arbitrary amplitudes. To show
629 how the pitch angle spectrogram evolves, drift velocities in parallel and perpendicular
630 directions with respect to the background magnetic fields have changed. No drifts in both
631 perpendicular and parallel to the background field lines (A). Only parallel drifts increased;
632 $0.3V_{th}$ (B), $0.6V_{th}$ (C) and $1.0V_{th}$ (D). For (E) and (F), perpendicular drift increased to $0.3V_{th}$
633 and $0.5V_{th}$ while parallel drift remained at $1.0V_{th}$. V_{th} denotes thermal velocity. The vertical
634 axis is for pitch angles, while the horizontal axis is for particle energies normalized by the
635 thermal energy.

636

637

638 Figure 4.

639 (A) Multiple Pi2 event (1, 2, 3, and 4 labelled in the Figure) with positive bay observed at low
640 latitude station (KUJ) at L=1.2 in the midnight sector (23:42 MLT at 15:00 UT). The figure,
641 from 1430 UT to 1600 UT 31 August 1986, was reproduced from [Saka et al., 2002]. (B)

642 Inclination angle of field lines in dipole coordinates along the satellite trajectories measured

643 by AMPTE CCE spacecraft. Inclination angle (θ) was defined as $\theta = \text{Tan}^{-1}\left(H/\sqrt{V^2 + D^2}\right)$.

644 H is positive northward parallel to the dipole axis, V is radial outward, and D is dipole east.

645 Vertical arrows denote dipolarization onset corresponding to the multiple Pi2; 1, 2, 3, and 4

646 in panel A. (C) Difference of duskward flux (counts/sample) (\mathbf{J}_-) and dawnward flux (\mathbf{J}_+) for

647 63-85 keV ion channel measured by AMPTE CCE spacecraft. (D) Same as for (C) but for
648 125-210 keV ion channel.

649 Radial distance (R) in Re, MLaT in degrees, and MLT at 14:30 UT, 15:00 UT and 16:00 UT
650 along satellite trajectory are shown in the bottom.

651

652

653 Figure 5.

654 A schematic illustration of particle measurement in X-Y plane of GSE coordinates; X is
655 earthward, Y is duskward in ecliptic plane. For the time interval of multiple Pi2 event when

656 the satellite was at 22 MLT, duskward flux represented by (\mathbf{J}_-) came from the earthward

657 sector and dawnward flux (\mathbf{J}_+) from tailward sector. $\mathbf{J}_- > \mathbf{J}_+$ because of the pressure

658 gradient positive earthward. Spatial gradient represented by solid line relaxed to dotted line.

659 Radial separation, $X_1 - X_2$, is either 1000 km or 1800 km for 63-85 keV ions or 125-210
660 keV ions, respectively.

661

662

663 Figure 6.

664 A schematic illustration of the field line deformations in the meridian plane associated with

665 the changing curvature radius of the field lines. The outer field lines marked by (1) changed

666 to field lines (2) by increasing their curvature radius to R1 (red-dashed circle) in association

667 with the relaxation of radial inhomogeneity, while the inner field lines marked by (3) moved

668 to field lines (4) of smaller curvature radius R2 (blue-dashed circle). This transition, (3) to (4),
669 may be caused by the radial gradient of magnetic pressures becoming steeper in association
670 with the inward compression of the field lines (see text). In the inset, flux tube deformations
671 in the equatorial cross section is illustrated at onset locations (field lines 1 and 2). Divergence
672 of perpendicular flows in dawn-dusk directions (solid arrows) produced dawn-dusk expansion
673 of flux tube (2) coincide with the shrinkage of stretched flux tube (1). Flux tube deformation
674 from 1 to 2 tended to preserve the total magnetic fluxes in the equatorial cross section.

675

676

677 Figure 7.

678 (A) Vertical component of $(rot \mathbf{J})_Z$ in the meridian chain along $300^\circ E$ for the interval from
679 1000 UT to 1500 UT, reproduced from Saka and Hayashi (2017). Dipolarization onset was
680 at 12:13 UT at this meridian. For the calculation of $(rot \mathbf{J})_Z$, vertical component data from
681 RES ($83.0^\circ N, 299.7^\circ E$), CBB ($76.6^\circ N, 301.2^\circ E$), CONT ($72.6^\circ N, 298.3^\circ E$), YKC ($68.9^\circ N,$
682 $298.0^\circ E$), FSIM ($67.2^\circ N, 290.8^\circ E$), FSJ ($61.9^\circ N, 295.5^\circ E$), and VIC ($54.1^\circ N, 296.7^\circ E$) along
683 the magnetic meridian $300^\circ E$ were used (see text). Positive for the clockwise rotation (CW)
684 of ionospheric currents and negative for the counterclockwise rotation (CCW) viewed from
685 above the ionosphere. Amplitudes are color-coded. The scale is shown on the right.
686 Demarcation lines separating CCW and CW in latitudes are marked by dashed line. The
687 demarcation line moved to poleward after the onset. Note that negative $(rot \mathbf{J})_Z$ in
688 poleward edge indicates smooth decrease of the Z amplitudes.

689

690 (B) Time progresses of the CW/CCW patterns are illustrated separately in five segments from
691 1 to 5 marked in Figure 7 (A). The figure demonstrates a progress of CW/CCW pair in time,
692 CW in the poleward and CCW in the equatorward. This pair developed its size after onset
693 showing poleward expansion. The meridional current associated with this pair of loop current,
694 if closed in the equatorial plane via the field-aligned currents, comprised the Bostrom type
695 current system.

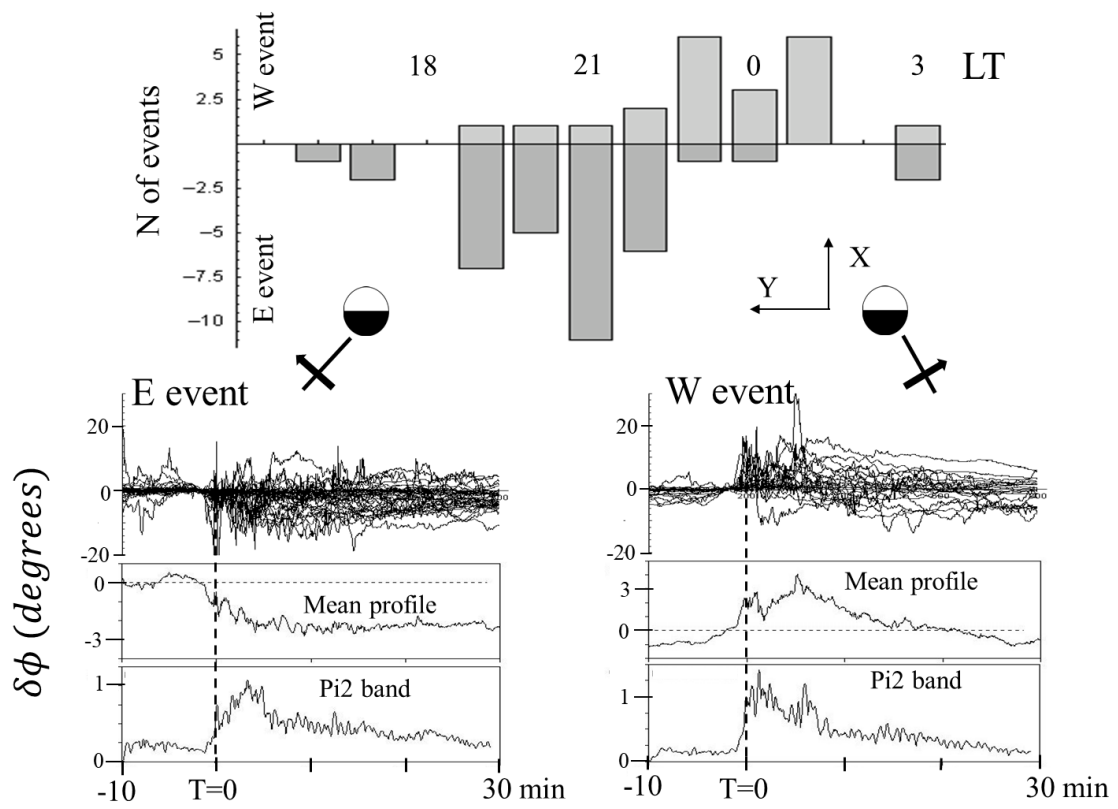


Figure 1

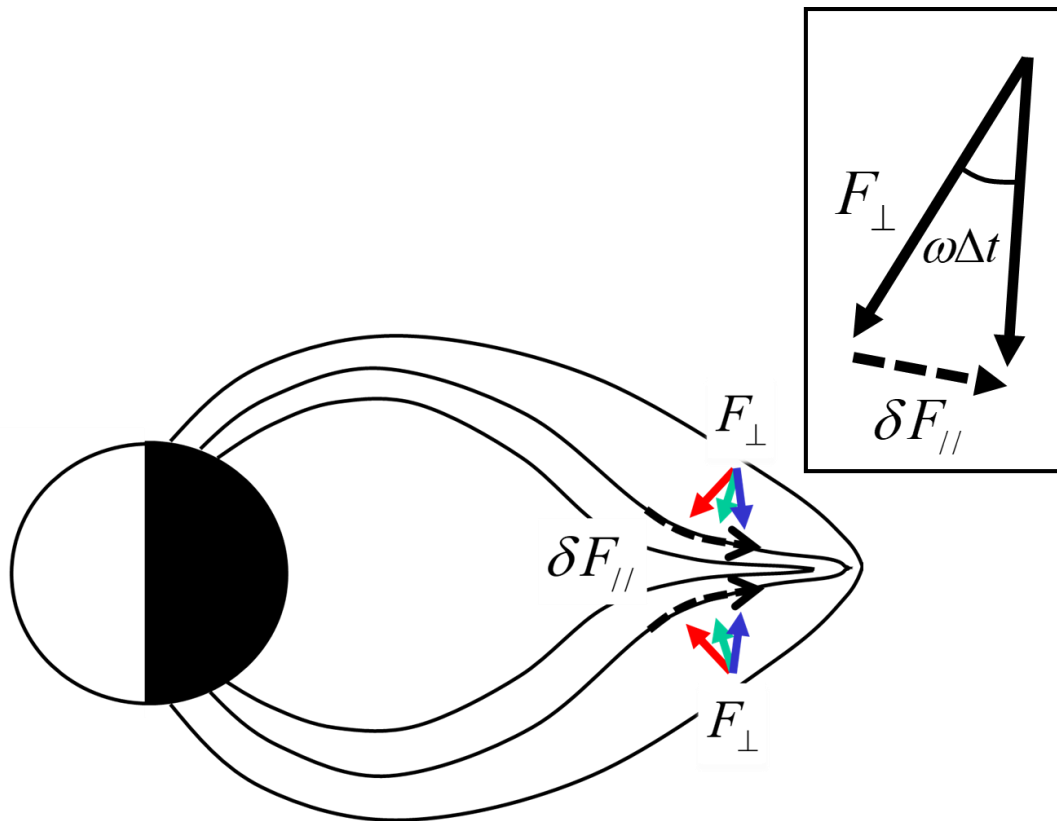


Figure 2

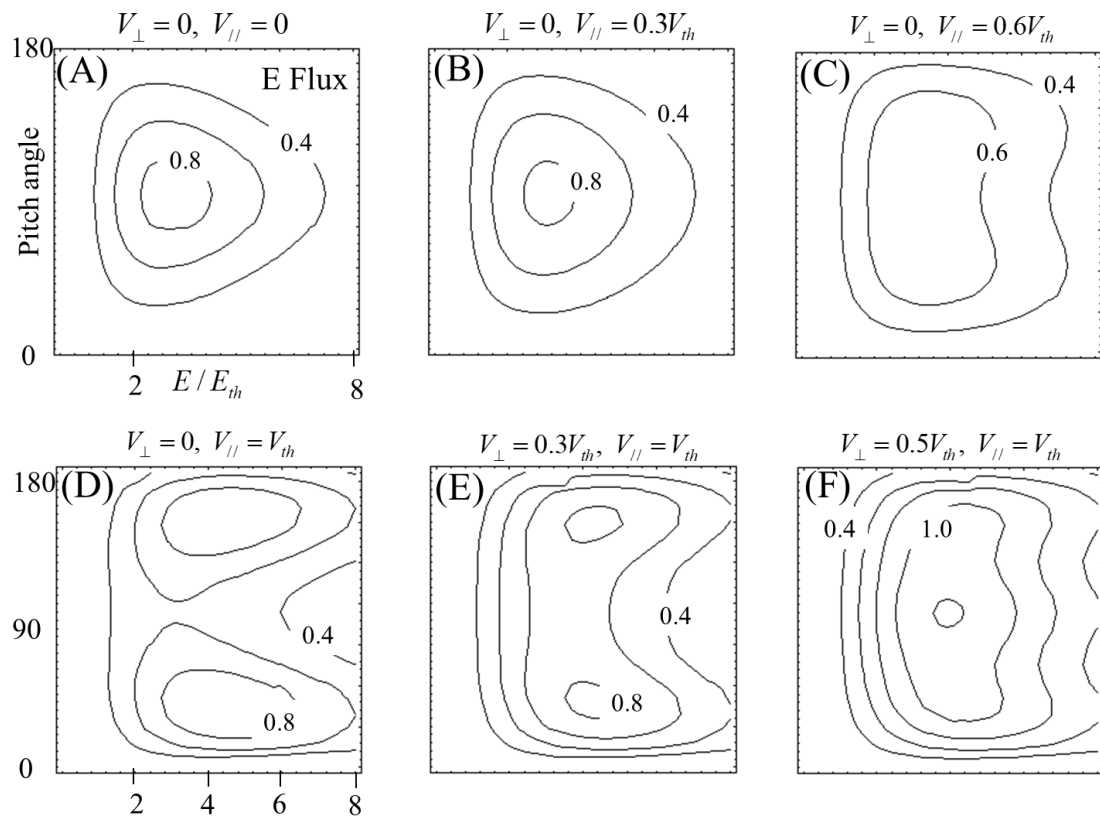


Figure 3

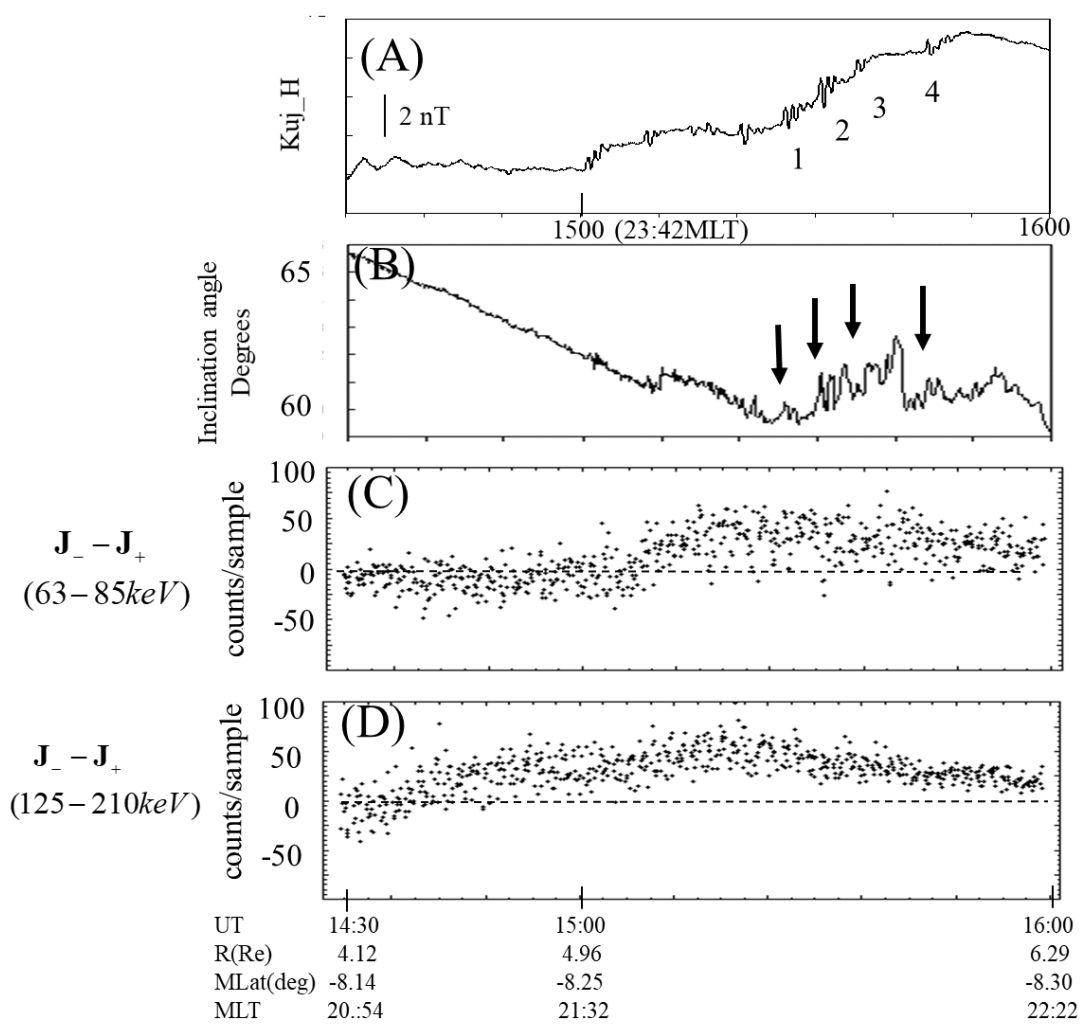


Figure 4

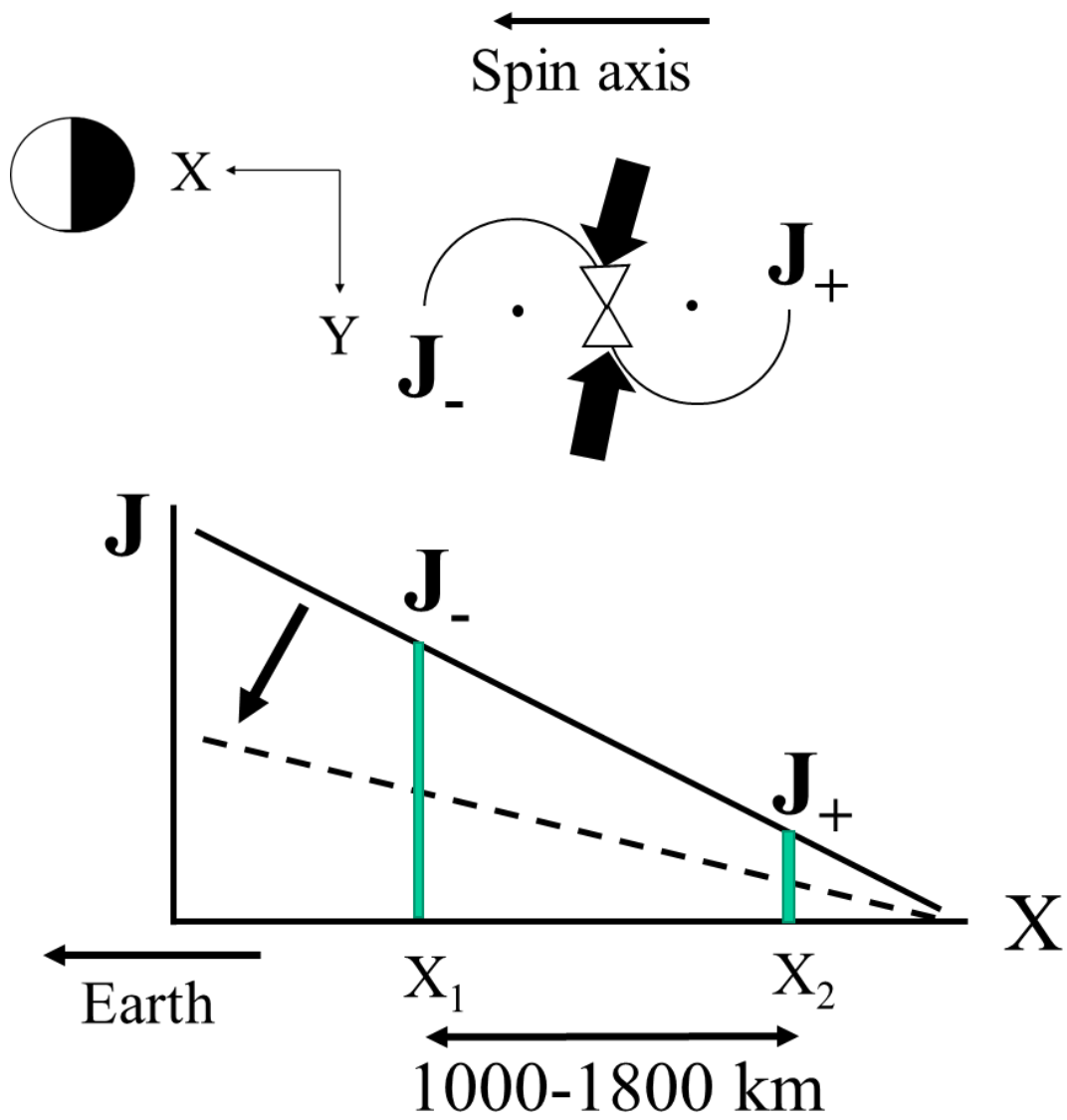


Figure 5

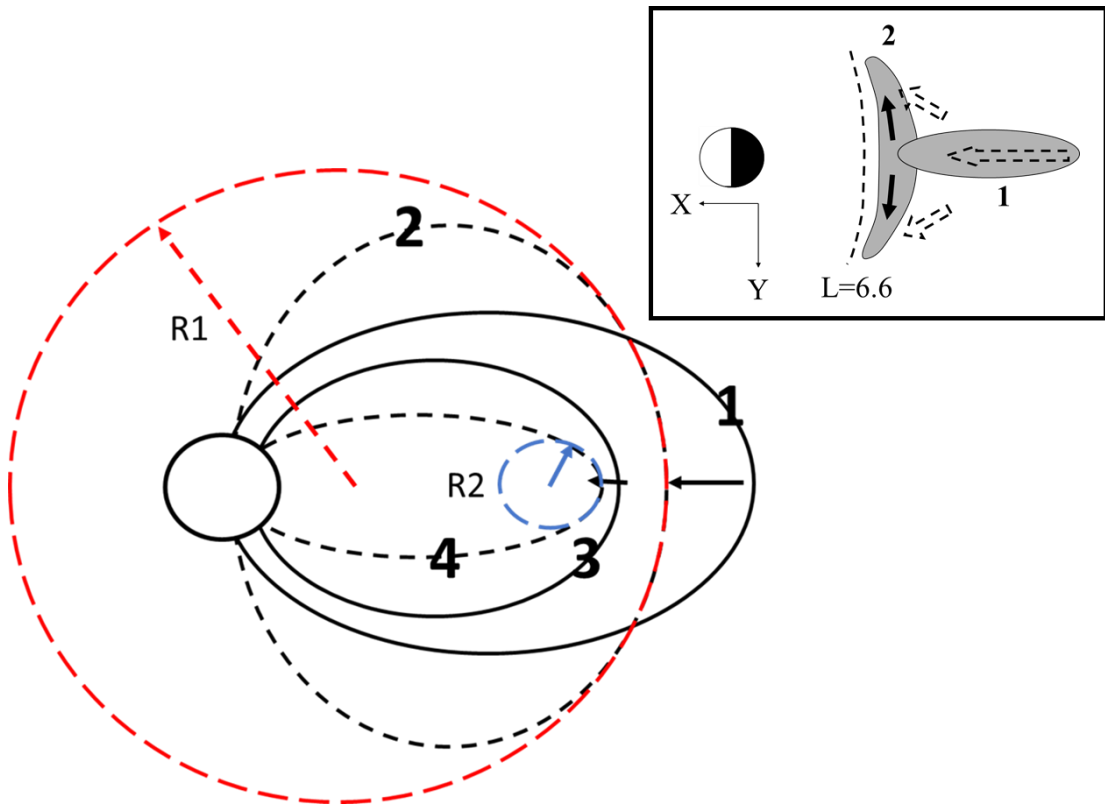


Figure 6

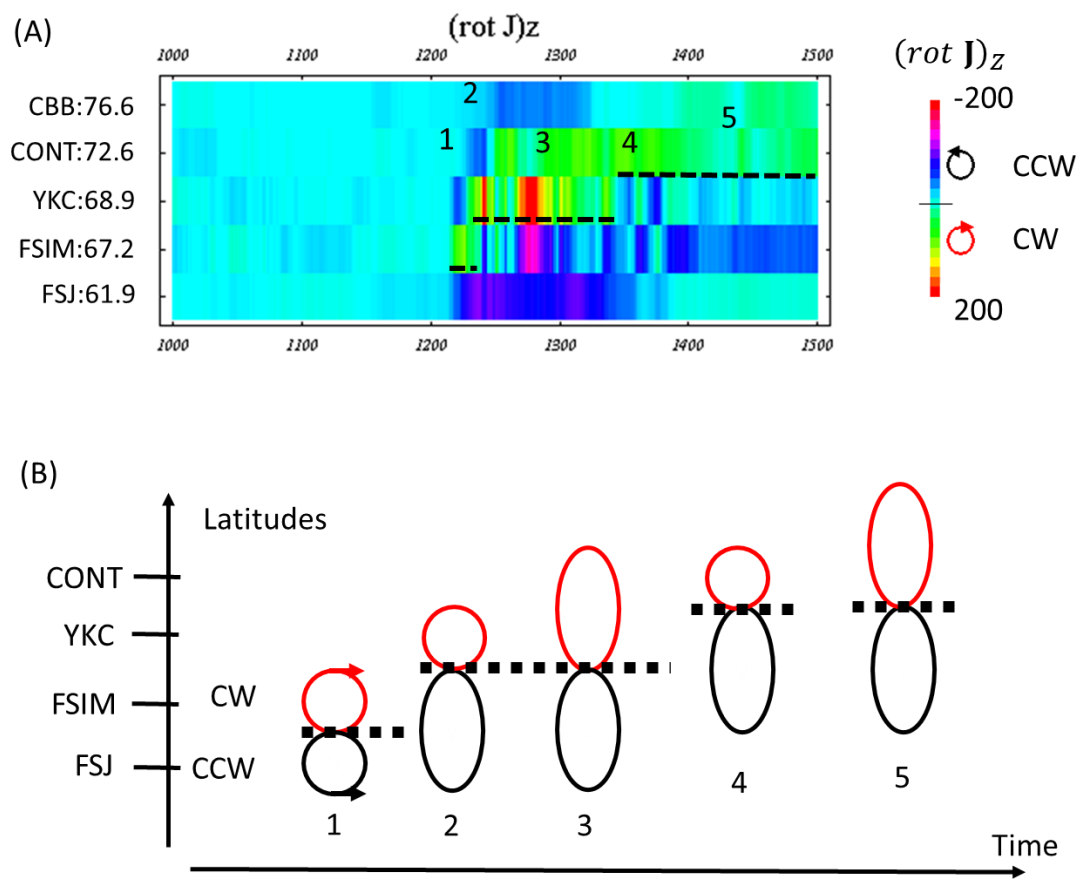


Figure 7